Article:

Boynton, R.J. orcid.org/0000-0003-3473-5403, Amariutei, O.A., Shprits, Y.Y. orcid.org/0000-0002-9625-0834 et al. (1 more author) (2019) The system science development of local time dependent 40 keV electron flux models for geostationary orbit. Space Weather, 17 (6). pp. 894-906. ISSN 1542-7390

https://doi.org/10.1029/2018sw002128

The system science development of local time dependent 40 keV electron flux models for geostationary orbit

R. J. Boynton,[1] O. A. Amariutei,[2] Y. Y. Shprits,[3,4] M. A. Balikhin,[1]

R. J. Boynton, Department of Automatic Control and Systems Engineering, University of Sheffield, Mappin Street, Sheffield S1 3JD, UK. (r.boynton@sheffield.ac.uk)

[1]Department of Automatic Control and

Abstract. At Geosynchronous Earth Orbit (GEO), the radiation belt/ring current electron fluxes with energies up to several hundred keV, can vary widely in Magnetic Local Time (MLT). This study aims to develop Nonlinear AutoRegressive eXogenous (NARX) models using system science techniques, which account for the spatial variation in MLT. This is difficult for system science techniques, since there is sparse data availability of the electron fluxes at different MLT. To solve this problem the data are binned from GOES 13, 14, and 15 by MLT, and a separate NARX model is deduced for each bin using solar wind variables as the inputs to the model. These models are then

Systems Engineering, University of Sheffield, Sheffield S1 3JD, United Kingdom.

[2]Department of Material Science and Engineering, University of Sheffield, Sheffield S1 3JD, United Kingdom.

[3]Helmholtz Centre Potsdam, GFZ German Research Centre for Geosciences, Potsdam, 14473, Germany.

[4]Department of Earth, Planetary, and Space Sciences, University of California, Los Angeles, 90095, CA, USA.

conjugated into one spatiotemporal forecast. The model performance statistics for each model varies in MLT with a Prediction Efficiency (PE) between 47% and 75% and a correlation coefficient (CC) between 51.3% and 78.9% for the period from 1 March 2013 to 31 December 2017.

1. Introduction

The radiation belt/ring current electrons with energies from tens of keV to several MeV can pose a serious threat to the satellites that our society is becoming increasingly reliant [*Horne et al.*, 2013a]. Therefore, models that are able to forecast the periods when the radiation belts or ring current electrons will be hazardous to these spacecraft are highly valuable to the satellite operators. Increases in the number of these electrons can lead to various problems on the satellite. High energy electrons, typically above 1 MeV, can cause deep dielectric charging, which can irrevocably damage the electronic components onboard the satellite [*Baker et al.*, 1987; *Wrenn et al.*, 2002; *Gubby and Evans*, 2002; *Lohmeyer and Cahoy*, 2013; *Lohmeyer et al.*, 2015]. 1 keV to 100 keV energy electrons can also be problematic to satellite operators, as they can contribute to surface charging, particularly at $\sim$ 10 keV, which interferes with the satellite electronic systems [*Olsen*, 1983; *Mullen et al.*, 1986; *O'Brien and Lemon*, 2007; *Thomsen et al.*, 2013; *Ferguson*, 2018; *Sarno-Smith et al.*, 2016]. This can potentially turn off vital systems onboard the spacecraft, which may be the cause of the anomaly on the Galaxy 15 spacecraft when it stopped responding to any ground commands [*Loto'aniu et al.*, Aug. 2015].

The dynamics of the radiation belts are known to be due to a balance between transport, acceleration and loss processes. The solar wind is known to drive the acceleration through wave-particle interactions and radial diffusion [*Friedel et al.*, 2002], while magnetopause shadowing [*Kim and Chan*, 1997; *Bortnik et al.*, 2006; *Turner et al.*, 2012] and precipitation through wave particle interaction [*Bailey*, 1968; *Bortnik et al.*, 2006] lead to the loss of these energetic electrons. However, the radiation belt models based on first principles struggle to provide accurate forecasts of the radiation belt electron fluxes [*Horne et al.*, 2013b].

An alternative approach to first principles based forecast models is the system identification or machine learning approach, where the models are automatically derived from input-output data by computer algorithms. These algorithms include linear prediction filters [*Baker et al.*, 1990; *Rigler et al.*, 2004], dynamic linear models [*Osthus et al.*, 2014], neural networks [*Koons and Gorney*, 1991; *Freeman et al.*, 1998; *Ling et al.*, 2010], and Nonlinear AutoRegressive Moving Average with eXogenous inputs (NARMAX) [*Wei et al.*, 2011; *Boynton et al.*, 2013a, 2015]. Neural networks and NARMAX methodologies are more suited to modelling the radiation belts, as the system is nonlinear with respect to the solar wind input. Linear prediction filters and dynamic linear models are only suitable for linear systems or local linearities within a nonlinear system. NARMAX and neural networks have both been shown to provide accurate models for geospace systems [*Freeman et al.*, 1998; *Boynton et al.*, 2011a, 2015], however, the advantages that NARMAX methodologies have over neural networks are that it is physically interpretable and less prone to overfitting. This study uses the NARMAX methodology to model the 40 keV electron fluxes observed by the Geostationary Operational Environmental Satellites (GOES), situated in Geostationary Earth Orbit (GEO).

The $>$ 2 MeV electrons at Geostationary Earth Orbit (GEO) have been modelled using NARMAX, which results in a high forecast accuracy and a forecast horizon of one day [*Boynton et al.*, 2015]. *Balikhin et al.* [2016] showed that the NARMAX model provides forecasts superior to the one provided by the National Oceanic and Atmospheric Administration (NOAA), which employs the model by *Baker et al.* [1990]. Higher energy electrons take time to be accelerated after responding to the solar wind variations [*Li et al.*, 2005; *Balikhin et al.*, 2012; *Boynton et al.*, 2013b]. This means that it is possible to forecast the dynamics of the high energy electrons further into the future than the lower energies. *Boynton et al.* [2016a] developed NARMAX models for the electron flux energy ranges observed by the third generation GOES (40 keV, 75 keV, 150 keV, 275 keV, 475 keV, $>$ 800 keV and $>$ 2 MeV). The developed models predict the daily averaged electron fluxes and were shown to provide an accurate forecast. Although the models provide a good forecast of the average conditions over a day in time and an orbit in space, they will be unable to forecast any spatial variations over the orbit. For the high energies, the electron fluxes are uniform in Magnetic Local Time (MLT) along the same drift shells. Due to the distorted dipole, the electron fluxes measured by GOES will vary in MLT as GEO does not follow drift shells or stay fixed at constant geomagnetic latitudes. The tens to hundreds of keV electrons that populate the ring current, provide the seed population of the radiation belts, and also drive the whistler mode chorus waves, which lead to both the acceleration of the energetic electrons and loss by precipitation. The injections of the tens to hundreds of keV electrons cause a fast localized electron flux variation on shorter time scales (less than 24 hours), which the *Boynton et al.* [2016a] models would average out. The Inner Magnetosphere Particle Transport and Acceleration Model (IMPTAM) [*Ganushkina et al.*, 2013, 2014, 2015] can provided a nowcast of the short time scale variations using current values of geomagnetic indices [*Ganushkina et al.*, 2015]. An empirical model of the 1 eV to 40 keV has been developed by [*Denton et al.*, 2016] as a function of local time, energy, and the strength of the solar wind electric field.

The aim of this study is to develop a reliable model that is able to forecast the short spatiotemporal variations of the 40 keV electron fluxes. The NARMAX methodology used to deduce the models is described in detail in Section 2, while the instrumentation and data are discussed in Section 3. In Section 4.1, the data are truncated every 1 hour MLT and 24 models are developed at each MLT. The performance and details of the models are discussed in Section 5 and the conclusions from this study are presented in Section 6.

2. NARMAX methodology

NARMAX is a system identification methodology [*Leontaritis and Billings*, 1985a, b] and was initially developed in the field of system science. In control theory, an application of system science, a mathematical model of the system is needed in order to build a robust controller. However, with complex engineering systems, the derivation of such a mathematical model from first principles often leads to assumption which are not valid and, hence, a poor controller. System identification aims to automatically derive a mathematical model that governs the system's dynamics from input-output data. NARMAX is able to deduce models for a wide range of nonlinear systems and was originally applied to complex engineering systems [*Billings*, 2013]. The potential of the methodology to develop nonlinear models from data has since been utilised by a diverse range of scientific fields. It has been used in analyzing the adaptive changes in the photoreceptors of Drosophila Flies [*Friederich et al.*, 2009], modelling the tide at the Venice Lagoon [*Wei and Billings*, 2006], the dynamics of Synthetic bioparts [*Krishnanathan et al.*, 2012], and the Belousov-Zhabotinsky chemical reaction [*Zhao et al.*, 2007]. In geospace the method was first used to model the Dst index and analyze the dynamics in the frequency domain [*Boaghe et al.*, 2001; *Balikhin et al.*, 2001]. A number of other Dst forecast models have also been developed, using single inputs [*Zhu et al.*, 2006], multiple inputs [*Zhu et al.*, 2007], and wavelets [*Wei et al.*, 2004]. *Boynton et al.* [2011b] utilized the NARMAX model structure detection methodology to identify a solar wind coupling function for geomagnetic storms, which was derived from first principles by *Balikhin et al.* [2010] and then employed as an input to model the Dst index [*Boynton et al.*, 2011a]. The method of using the physical interpretability of the NARMAX model structure detection has since been used in many other studies to identify relationships between the solar wind and various aspects of the magnetosphere. Examples include studies of SYM-H index *Beharrell and Honary* [2016], proton fluxes at GEO [*Boynton et al.*, 2013c], the electron fluxes [*Balikhin et al.*, 2011; *Boynton et al.*, 2013b], and electron flux dropouts at GEO [*Boynton et al.*, 2016b] and at the GPS orbit [*Boynton et al.*, 2017].

A Multi-Input Single-Output (MISO) NARMAX model was used in this study to model the electron fluxes. This is represented by

$$\begin{aligned}\hat{y}(t) \;=\; & F[y(t-1),...,y(t-n_y),\\ & u_1(t-1),...,u_1(t-n_{u_1}),...,\\ & u_m(t-1),...,u_m(t-n_{u_m}),...,\\ & e(t-1),...,e(t-n_e)]\end{aligned} \tag{1}$$

where an estimate of the output $\hat{y}$ at time t is a nonlinear function F of past outputs y, inputs u, and residual, $e = y - \hat{y}$. m is the number of system inputs and n_y, n_{u_1},..., n_{u_m}, n_e are the maximum time lags for the output, each of the m inputs, and the error, respectively.

For this study, the nonlinear function F was chosen to be a nonlinear polynomial. When this polynomial is expanded there will be many monomials, most of which have no influence on the system and keeping them would most likely lead to an overfit model. To overcome this problem, *Billings et al.* [1988] developed the Forward Regression Orthogonal Least Squares (FROLS) algorithm, which detects a small model structure from the larger polynomial and estimates the coefficients for each of the detected monomials. The model structure is detected using the Error Reduction Ratio (ERR), which indicates the influence that a monomial has on the output variance. This study employs the Iterative Orthogonal Forward Regression (IOFR) algorithm, which is a variant of the original FROLS. This is more likely to detect the optimal model when the data is oversampled [*Guo et al.*, 2014]. A more detailed description of the NARMAX methodology is described by *Billings* [2013] or *Boynton et al.* [2018].

3. Instruments and data

The data used in this study are from the third generation GOES MAGnetospheric Electron Detector (MAGED) [*Hanser*, 2011]. The data for these instruments can be accessed from http://www.ngdc.noaa.gov/stp/satellite/goes/dataaccess.html. The MAGED has 9 telescopes covering a range of different directions and measures the differential electron fluxes in 5 energy channels: 40 keV, 75 keV, 150 keV, 275 keV and 475 keV [*Hanser*, 2011]. The time period used to derive and test the models was from 1 January 2011 to 13 December 2017. Three GOES spacecraft have carried this instrument, GOES 13, 14 and 15. These spacecraft were situated at GEO at various longitudes over North America and were in operation at different times during this period.

The following MAGED data have been removed from this study due to anomalies: GOES 13 on telescope 6 throughout this period; GOES 14 between 30 March 2010 and 2 May 2010 on telescopes 2, 5, and 8; and GOES 15 between 25 November 2017 and 31 December 2017 on telescope 1.

Solar wind data were used as input data for training and testing the models. The 1-minute solar wind velocity, density and Geocentric Solar Magnetospheric (GSM) IMF data were obtained from the OMNI website (http://omniweb.gsfc.nasa.gov/ow_min.html).

4. Individually binned MLT models

The method of choice of applying system identification to spatially varying systems with different physics occurring in different locations is often to bin the data into different spatial bins and then develop an individual model for each of the spatial bins. This raises two questions: What should be the size of the spatial bin? And what should be the temporal resolution of the data? With most system science applications to geospace the temporal resolution is usually the resolution of the output, e.g., the Dst index has a resolution of 1 hour and is modelled with a 1 hour resolution [*Klimas et al.*, 1996]. The temporal sampling frequency should be fast enough to extract the desired information from the signal. Shannon's theorem states that if the desired information has a frequency f_c then to recover the desired information a sampling frequency of at least $2f_c$ is required. Oversampling is not beneficial for system science modelling as the model will require the inclusion of more lags, which will overcomplicate the model and increases the computation time. The same is true for sampling the spatial frequency. Therefore, we need to know the spatial and temporal frequency of the high flux variations of keV electrons. The electron losses are due to either precipitation to the atmosphere from pitch angle scattering or magnetopause shadowing with radial diffusion. Both these mechanisms should occur at a wide range of MLT but take place over a short time period. Increases in electron flux from radial diffusion will transpire over longer periods of time and increases from enhanced convection will occur over a wide range of MLT at the same time. The mechanism that leads to the high spatiotemporal frequency variations is due to the substorm associated injections from the plasma sheet. The spatial and temporal scales at which injections can occur are known to vary from one substorm to another [*Sergeev and Tsyganenko*, 1982; *Ganushkina et al.*, 2013; *Gabrielse et al.*, 2014], and further studies are required to determine the azimuthal extent of the injection fronts. However, this study still requires a spatiotemporal sampling frequency to deduce the electron flux model.

Figure 1 shows the 40 keV electron flux from the MAGED onboard GOES 13 (blue), 14 (orange) and 15 (yellow) from 27 October 2012 to 29 October 2012 and when each of the spacecraft is at midday (GOES 13 - blue dashed, 14 - orange dashed, and 15 - yellow dashed) and midnight (GOES 13 - blue dot dashed, 14 - orange dot dashed, and 15 - yellow dot dashed). During this period, GOES 13 is 1 hour MLT ahead of GOES 14 and 4 hours MLT ahead of GOES 15. Up until 06 UTC on 28 October 2012, all three measurements follow the same trend, with GOES 13 and 14 recording almost exactly the same values and GOES 15 having a small offset. GOES 13 and 14 then observe an increase of electron fluxes of approximately one order of magnitude at a post midnight MLT that lasted 2 hours in time, which is not measured by GOES 15 at the pre midnight MLT. This spatiotemporally localized bump in the electron flux time series is most likely caused by an injection of energetic electrons from the plasma sheet. There are then a series of peaks in the electron fluxes observed by all three spacecraft with GOES 13 and

14 again observing almost exactly the same values and GOES 15 having an offset. Then another bump in the fluxes probably caused by an injection was observed by GOES 13 and 14 but not GOES 15. This increase lasted ~ 2 hours and was observed by GOES 13 from 2.2 to 4.3 MLT and by GOES 14 from 1.3 to 3.4 MLT, while at the same time GOES 15 moved from 22.2 to 0.3 MLT. These two potential injection structures both had a temporal length of ~ 2 hours and a spatial width larger than 1 hour MLT, but did not extend 4 hours MLT back from GOES 13 to GOES 15. Inspecting longer periods of data in which all three spacecraft are in operation does show structures with narrower temporal widths but a structure observed by the middle spacecraft is almost always observed by one of the other two spacecraft. Therefore, a sampling of 1 hour MLT and 1 hour time was selected as a good compromise between sampling the majority of high spatiotemporal frequency injections and model complexity since a higher resolution will lead to more temporal lags. Electron flux enhancements through convection and radial diffusion will both be oversampled in space, since convection will occur simultaneously over a broad range of MLT and radial diffusion will take place at all MLT simultaneously.

4.1. Spatiotemporally sampled 40 keV electron flux model

The GOES 13, 14 and 15 40 keV electron flux data from the MAGED were sampled at 1 hour time resolution and at 1 hour MLT, smoothing over 12 minutes MLT around each hour MLT, and averaging over the 9 telescopes from each spacecraft with pitch angles between 20° and 160° (excluding the errors mentioned in Section 3). This resulted in 24 time series datasets for each MLT, which were then individually modelled using the NARMAX methodology described in Section 2. Here, the time series of the electron flux at one of the 24 MLTs is the output data, $J(MLT, t)$. Most of the points in each of the time series datasets were empty since for the majority of the time there will be no spacecraft in the MLT bin. The input data employed were the solar wind velocity $v(t)$, density $n(t)$, square root of the pressure $\sqrt{p}(t)$, and the IMF factor $B_f(t) = B_T(t)\sin^6(\theta(t)/2)$ (where $B_T(t) = \sqrt{B_y(t)^2 + B_z(t)^2}$ and $\theta = \tan^{-1}(B_y(t)/B_z(t))$) deduced by *Boynton et al.* [2011b] and *Balikhin et al.* [2010]. The output lags were selected as the value 24 hours previous. This is the most consistent data point that will be available, since any other output lag will most likely be empty in the constructed time series dataset. The input time lags were selected as 1, 3, 5,..., 23 hours as it has been shown that 10 to 100 keV electrons have short response times with solar wind variations compared to MeV electrons [*Li et al.*, 2005; *Boynton et al.*, 2013b]. The noise terms were not included in the model because these data were sparse. This reduces the NARMAX model to the following NARX model:

$$\begin{aligned}\hat{J}(MLT,t) \; = \; & F[J(MLT,t-24),\\ & v(t-1), v(t-3), ..., v(t-23),\\ & n(t-1), n(t-3), ..., n(t-23),\\ & \sqrt{p}(t-1), \sqrt{p}(t-3), ..., \sqrt{p}(t-23),\\ & B_f(t-1), B_f(t-3), ..., B_f(t-23)] \qquad (2)\end{aligned}$$

The nonlinear function F was chosen to be a third degree polynomial, thus, the model can include linear monomials of the lagged inputs and outputs as well as cross coupled combinations of the lagged inputs and outputs.

The IOFR algorithm was run for each of the 24 datasets using the same NARX model on data from 00:00 UTC 1 January 2011 to 23:00 UTC 28 February 2013. These models were then assessed statistically on data from 1 March 2013 to 31 December 2017 using the Prediction Efficiency (PE), Eq. (3), Correlation Coefficient (CC), Eq. (4), Mean Square Error (MSE), and the variance of the observed flux, which are commonly used to assess models [*Temerin and Li*, 2006; *Li*, 2004; *Boynton et al.*, 2011a; *Wei et al.*, 2004; *Boynton et al.*, 2015; *Rastatter et al.*, 2013]. The equations for PE and CC are:

$$E_{PE} = \left[1 - \frac{\sum_{t=1}^{N} \left[(y(t) - \hat{y}(t))^2 \right]}{\sum_{t=1}^{N} \left[(y(t) - \bar{y})^2 \right]} \right] 100\% \tag{3}$$

$$\rho_{y\hat{y}} = \frac{\sum_{t=1}^{N} \left[(y(t) - \bar{y}) \left(\hat{y}(t) - \bar{\hat{y}} \right) \right]}{\sqrt{\sum_{t=1}^{N} \left[(y(t) - \bar{y})^2 \right] \sum_{t=1}^{N} \left[\left(\hat{y}(t) - \bar{\hat{y}} \right)^2 \right]}} 100\% \tag{4}$$

$$E_{MSE} = \sum_{t=1}^{N} \left[(y(t) - \hat{y}(t))^2 \right] \tag{5}$$

Here, E_{PE} is the PE, ρ is the CC, E_{MSE} is the MSE, $y(t)$ is the measured output at time t, $\hat{y}$ is the estimated output from the model, N is the length of the data and the bar signifies the average. The model performance statistics of each of these models are displayed in Table 1. The PE for each model varies by 47% and 75% while the CC varies between 51.3% and 78.9%. The highest PE and CC occur at 09 MLT and decreases to the lowest PE and CC at 22 MLT. The MSE and variance have a similar sinusoidal pattern with both having a minimum at 16 MLT of 0.045 and 0.090 respectively and the MSE having a maximum at 01 MLT of 0.208, while the maximum of the variance is 0.288 at 05 MLT.

Figure 2 shows the model estimate of the 40 keV electron fluxes from 1 November 2017 to 30 November 2017 for different MLT. During this period, the model forecasts a number of enhancements that are most intense at dawn MLTs and are lowest at evening MLTs. Even though all the estimates at each MLT are from a different model, the structure of the plots is consistent. A surface plot of the forecast is good for showing the evolution of the fluxes but will be not be able to illustrate the performance of the model compared to the observed fluxes, since, at each point in time, there will only be a few MLT measurements. Figure 3 (a) shows a comparison of the model with GOES 13 measurements for the same 1 November 2017 to 30 November 2017 period displayed in Figure 2. The 1 minute GOES 13 data is presented in blue, the spatiotemporal sampled GOES data in red and the model forecast at the GOES 13 location shown in green. Panel (b) displays the error between the sampled GOES 13 40 keV electron flux and the model forecast at the GOES 13 location. The model forecast is shown to follow the enhancements and decreases of the measured electron flux data with a MSE of 0.083 $\log_{10}$ for the displayed period. The model is able to forecast the large variations, for example, the decrease and the increase on 3 November 2017, but struggles to reproduce the higher frequency variations. A video of the variations in electron flux at different MLT for the period in Figures 2 and 3 are in the supplementary material.

5. Discussion

One advantage of NARMAX methodologies over neural network machine learning techniques, other than its resilience to overfitting, is that the models are physically interpretable. The resulting models from the NARMAX algorithm are polynomials consisting of approximately 5 to 20 monomials [*Billings*, 2013]. By inspecting the monomials that were selected for the model, it is possible to gain some understanding into the underlying physical processes of the system [*Balikhin et al.*, 2010; *Boynton et al.*, 2011b; *Balikhin et al.*, 2012; *Boynton et al.*, 2013b; *Billings*, 2013]. The model for the 01 MLT 40 keV electron fluxes is

$$\begin{aligned}
\hat{J}(01MLT,t) \;=\;& 3.21\times10^{-4}B_f(t-1)v(t-1)+2.57+1.78\times10^{-3}v(t-5)\\
&+4.02\times10^{-2}B_f(t-5)-4.51\times10^{-3}B_f^2(t-1)\\
&+1.07\times10^{-2}J^2(01MLT,t-24)-1.46\times10^{-1}p(t-3)\\
&+5.91\times10^{-2}B_f(t-21)+4.72\times10^{-1}\sqrt{p}(t-3)+1.47\times10^{-3}v(t-17)\\
&-4.69\times10^{-3}B_f(t-20)B_f(t-21)-3.74\times10^{-2}B_f(t-1)\sqrt{p}(t-1)\\
&+7.35\times10^{-2}B_f(t-13)-3.41\times10^{-2}B_f(t-13)\sqrt{p}(t-14)\\
&-5.87\times10^{-3}B_f^2(t-7)+5.16\times10^{-2}B_f(t-7)\\
&-1.34\times10^{-6}v(t-8)v(t-9) \qquad (6)
\end{aligned}$$

One interesting point about the models deduced by the algorithm using the initial NARX model structure in Eq. (2) is that only the 01 MLT, 04 MLT, and 18 MLT models out of the 24 models included the autoregressive $J(MLT, t-24)$ term out of the 24 models. The autoregressive monomials in each of the three NARX models only have a small contribution to the variance of the output, indicated by the small ERR. The other models, with no past output terms and only consisting of exogenous terms, are known as Volterra Series models. The lack of autoregressive terms and the small ERR contribution when they are selected in the model means that the hourly MLT electron flux changes significantly from their value 24 hours ago.

The variable that is selected in all the models, and appears as a factor of the monomial that has the highest ERR in each of the models, is the IMF factor B_f. The monomial with the highest ERR controls most of the output variance. The solar wind velocity is the second most selected variable and it is in all the models in either the first or second highest ERR monomial, often coupled with B_f. The square root of the solar wind pressure is chosen by the algorithm in 23 of the models (not the 23 MLT model) and the solar wind density is only selected in 14 of the models but both are rarely selected in the top five terms in order of ERR (three times for both pressure and density) and, thus, only have a small contribution to the variance of the output.

The IMF factor B_f was automatically identified in a solar wind-magnetosphere coupling function by using the NARMAX FROLS methodology and then derived analytically from first principles by *Balikhin et al.* [2010]. This derivation is based on the geometry of the dayside magnetosphere reconnection with the solar wind. Therefore, the fact that the models attribute most of the variation of the electron fluxes to the IMF factor implies that the reconnection is the most important process. On the surface, this is in contrast to the higher energies where solar wind velocity [*Paulikas and Blake*, 1979] or density [*Balikhin et al.*, 2011] was found to have the most influence. However, these studies investigated the daily averages of electron fluxes and solar wind, which will average out the turning of the IMF southward over the day, since these time scales are quite short ($\sim$ 1 hour). With the increased temporal resolution the turning of the IMF southward will not be averaged out and and will have more influence. This averaging out over the timescales of the IMF variations is also true for the study by *Boynton et al.* [2013b] where they also found that southward IMF only had a small influence on the daily averaged 10 to 100 keV electron fluxes. For example, if there is a high velocity solar wind event taking place over several days and there are several periods of time when the IMF is southward for an hour, the IMF may average out to be insignificant, while the velocity remains high. Therefore, choosing a different time resolution may change the importance of the parameters.

The performance of the different electron flux models show a pattern with the MLT, with the highest performance in terms of CC and PE in the late morning and the lowest performance just before midnight. The lower performance just before midnight could be due to the model not performing very well at forecasting the higher spatiotemporal frequency injections that occur in this region. The MSE also exhibits a pattern with MLT but it is shifted compared to PE and CC, with the highest MSE at 01 MLT and the lowest at 15 and 16 MLT. The shift between PE and CC variation with MLT and the MSE MLT variation is mainly due to the difference in the electron flux variance at each MLT, since both PE and CC are normalized by the variance of the measured electron fluxes.

The highest performance in terms of PE and CC occur at dayside MLTs, where the increases in the fluxes will mostly be due to convection or radial diffusion and are unlikely to be caused by substorm particle injections. From Figure 3, the model estimates the majority of the structures that last over half a day but a magnified figure would show more detail. Figure 4 displays two magnified sections of Figure 3, panel (a) from 10 November 2017 to 12 November 2017, and panel (b) from 20 November 2017 to 22 November 2017. The Figures show that the model follows the general trend of the measured GOES 13 data during this period. There is a sharp peak in the 1 minute GOES 13 measurements (blue) on 10 November 2017 at 0400 UTC, which is averaged out in the sampled GOES measurement (red), however, the model (green) does show an increase. Overall, the model underperforms in forecasting the high spatial and temporal frequency variations, such as the three peaks between 0600-1800 UTC on 11 November 2017, but follows the slower variations. An increased temporal resolution of 30 minutes may help in identifying the fast substorm associated injections. The inputs to the model are measured at L1 and using a 1 hour time lag in the model, which may lead to changes in the solar wind occurring inside the hour. For example, a fast flow of solar wind can transit from L1 to the bow shock in under 30 minutes, which will cause a change in the magnetosphere that the 1 hour lags in the model will be unable to take into account. Therefore, in the training of the model, these changes in solar wind cannot be identified as drivers of the changes in the electron fluxes. However, a consequence of including shorter lags in the model will be to reduce the forecast horizon of the model. Also, the averaging of the solar wind over the hour, particularly the fast turning of the solar wind southward, may nullify the drivers of the substorm, therefore, it will not be identified in the model. This problem could be solved by including the maximum of the value of the solar wind parameters as inputs as well as the average value, however, this would increase the computational complexity of identifying the model due to an increased amount of monomials to search through.

Another option to spatially model the electron fluxes is to employ MLT as an input into the model, rather than sampling the data in space and developing a separate model for each spatial bin. However, this approach was not selected because at different MLTs there should be different dynamics, and it would be better to isolate the individual physical processes in the different models corresponding to each region.

A model of the 40 keV electron fluxes through all MLTs at geostationary orbit is not only useful to satellite operators, who would be able to have a greater situational awareness of the environment and be able to apply any mitigation procedures to help protect their space based assets. The model could also be used as an outer boundary condition to physics based radiation belt models such as the Versatile Electron Radiation Belt (VERB) model [*Subbotin et al.*, 2011], Comprehensive Inner Magnetosphere-Ionosphere (CIMI) model [*Fok et al.*, 2014] or IMPTAM [*Ganushkina et al.*, 2015].

The models developed in this study have been implemented to run in real time. A figure of the real time output of this model is shown in Figure 5, which shows the model output across all MLT in panel (a), the model output at the location of GOES 15 vs GOES 15 data, and (c) the error between the measured and model for March 2019. The model performance for this period were a PE of 48.5% and a CC of 66.3%. The data gap at the start of the month is due to a missing solar wind inputs, which were not available from NOAA Space Weather Prediction Center (SWPC) at the time the forecast was made.

6. Conclusions

A data based spatiotemporal model has been developed for the 40 keV electron fluxes at GEO. This model is comprised of 24 individual NARX models of the form shown in Equation (2), where the output of each model is the electron fluxes for that region of space in MLT at GEO. When the 24 models are conjugated together into the final model, they give a forecast of the spatiotemporal evolution of the 40 keV electron fluxes at GEO. At this energy, the electron fluxes can vary significantly over a narrow range of MLTs due to substorm associated injections making it very challenging to model. The development of a data based model using system science techniques is complicated by the sparse availability of the electron fluxes at different MLT. This problem was solved by binning the data from GOES 13, 14, and 15 by MLT and then deducing a separate model for each bin then conjugating these to produce one spatiotemporal forecast. The performance of this forecast was then assessed on a period from 1 March 2013 to 31 December 2017 where the PE varied between 47% and 75% and the CC varied between 51.3% and 78.9% at different MLTs.

The models developed in this study will be implemented online at the University of Sheffield Space Weather Website (http://www.ssg.group.shef.ac.uk/USSW2/UOSSW.html) to provide a real time forecast of the GEO 40 keV electron fluxes through all MLTs. This will allow both satellite operators and scientists to have access to the outputs of the models, which will also be archived.

Acknowledgments. The MAGED data can be accessed from http://www.ngdc.noaa.gov/stp/satellite/goes/dataaccess.html. The solar wind data and geomagnetic indices data were from the OMNI website (http://omniweb.gsfc.nasa.gov/ow_min.html). The real time data were from the NOAA SWPC. The work was performed within the project Rad-Sat and has received financial support from the UK NERC under grant NE/P017061/1.

References

Bailey, D. K., Some quantitative aspects of electron precipitation in and near the auroral zone, *Rev. Geophys.*, *6*(3), 289–346, 1968.

Baker, D., R. Belian, P. Higbie, R. Klebesadel, and J. Blake, Deep dielectric charging effects due to high-energy electrons in earth's outer magnetosphere, *Journal of Electrostatics*, *20*(1), 3–19, 1987.

Baker, D. N., R. L. McPherron, T. E. Cayton, and R. W. Klebesadel, Linear prediction filter analysis of relativistic electron properties at 6.6 re, *J. Geophys. Res.*, *95*(A9), 15,133–15,140, 1990.

Balikhin, M. A., O. M. Boaghe, S. A. Billings, and H. S. C. K. Alleyne, Terrestrial magnetosphere as a nonlinear resonator, *Geophys. Res. Lett.*, *28(6)*, 1123–1126, 2001.

Balikhin, M. A., R. J. Boynton, S. A. Billings, M. Gedalin, N. Ganushkina, D. Coca, and H. Wei, Data based quest for solar wind-magnetosphere coupling function, *Geophys. Res. Lett.*, *37*(24), L24,107, 2010.

Balikhin, M. A., R. J. Boynton, S. N. Walker, J. E. Borovsky, S. A. Billings, and H. L. Wei, Using the narmax approach to model the evolution of energetic electrons fluxes at geostationary orbit, *Geophys. Res. Lett.*, *38*(18), L18,105, 2011.

Balikhin, M. A., M. Gedalin, G. D. Reeves, R. J. Boynton, and S. A. Billings, Time scaling of the electron flux increase at geo: The local energy diffusion model vs observations, *J. Geophys. Res.*, *117*(A10), A10,208–, 2012.

Balikhin, M. A., J. V. Rodriguez, R. J. Boynton, S. N. Walker, H. Aryan, D. G. Sibeck, and S. A. Billings, Comparative analysis of noaa refm and snb3geo tools for the forecast of the fluxes of high-energy electrons at geo, *Space Weather*, *14*(1), 2015SW001,303–, 2016.

Beharrell, M. J., and F. Honary, Decoding solar wind-magnetosphere coupling, *Space Weather*, *n/a*, 2016SW001,467–, 2016.

Billings, S., M. Korenberg, and S. Chen, Identification of non-linear output affine systems using an orthogonal least-squares algorithm., *Int. J. of Systems Sci.*, *19*, 1559–1568, 1988.

Billings, S. A., *Nonlinear System Identification: NARMAX Methods in the Time, Frequency, and Spatio-Temporal Domains*, Wiley, 2013.

Boaghe, O. M., M. A. Balikhin, S. A. Billings, and H. Alleyne, Identification of nonlinear processes in the magnetospheric dynamics and forecasting of dst index, *J. Geophys. Res.*, *106(A12)*, 30,047–30,066, 2001.

Bortnik, J., R. M. Thorne, T. P. O'Brien, J. C. Green, R. J. Strangeway, Y. Y. Shprits, and D. N. Baker, Observation of two distinct, rapid loss mechanisms during the 20 november 2003 radiation belt dropout event, *J. Geophys. Res.*, *111*(A12), A12,216–, 2006.

Boynton, R., M. Balikhin, H.-L. Wei, and Z.-Q. Lang, *Machine Learning Techniques for Space Weather*, chap. Applications of NARMAX in Space Weather, pp. 203–237, Elsevier, 2018.

Boynton, R. J., M. A. Balikhin, S. A. Billings, A. S. Sharma, and O. A. Amariutei, Data derived narmax dst model, *Annales Geophysicae*, *29*(6), 965–971, doi:10.5194/angeo-29-965-2011, 2011a.

Boynton, R. J., M. A. Balikhin, S. A. Billings, H. L. Wei, and N. Ganushkina, Using the narmax ols-err algorithm to obtain the most influential coupling functions that affect the evolution of the magnetosphere, *J. Geophys. Res.*, *116*(A5), A05,218, 2011b.

Boynton, R. J., M. A. Balikhin, S. A. Billings, and O. A. Amariutei, Application of nonlinear autoregressive moving average exogenous input models to geospace: advances in understanding and space weather forecasts, *Ann. Geophys.*, *31*(9), 1579–1589, 2013a.

Boynton, R. J., M. A. Balikhin, S. A. Billings, G. D. Reeves, N. Ganushkina, M. Gedalin, O. A. Amariutei, J. E. Borovsky, and S. N. Walker, The analysis of electron fluxes at geosynchronous orbit employing a narmax approach, *J. Geophys. Res. Space Physics*, *118*(4), 1500–1513, 2013b.

Boynton, R. J., S. A. Billings, O. A. Amariutei, and I. Moiseenko, The coupling between the solar wind and proton fluxes at geo, *Ann. Geophys.*, *31*(10), 1631–1636, 2013c.

Boynton, R. J., M. A. Balikhin, and S. A. Billings, Online narmax model for electron fluxes at geo, *Ann. Geophys.*, *33*(3), 405–411, 2015.

Boynton, R. J., M. A. Balikhin, D. G. Sibeck, S. N. Walker, S. A. Billings, and N. Ganushkina, Electron flux models for different energies at geostationary orbit, *Space Weather*, *14*(10), 2016SW001,506–, 2016a.

Boynton, R. J., D. Mourenas, and M. A. Balikhin, Electron flux dropouts at geostationary earth orbit: Occurrences, magnitudes, and main driving factors, *J. Geophys. Res. Space Physics*, *121*(9), 2016JA022,916–, 2016b.

Boynton, R. J., D. Mourenas, and M. A. Balikhin, Electron flux dropouts at l 4.2 from global positioning system satellites: Occurrences, magnitudes, and main driving factors, *J. Geophys. Res. Space Physics*, *122*(11), 11,428–11,441, doi:10.1002/2017ja024523, 2017.

Denton, M. H., M. G. Henderson, V. K. Jordanova, M. F. Thomsen, J. E. Borovsky, J. Woodroffe, D. P. Hartley, and D. Pitchford, An improved empirical model of electron and ion fluxes at geosynchronous orbit based on upstream solar wind conditions, *Space Weather*, *14*(7), 511–523, doi:10.1002/2016sw001409, 2016.

Ferguson, D. C., Chapter 15 - extreme space weather spacecraft surface charging and arcing effects, in *Extreme Events in Geospace*, edited by N. Buzulukova, pp. 401–418, Elsevier, 2018.

Fok, M. C., N. Y. Buzulukova, S. H. Chen, A. Glocer, T. Nagai, P. Valek, and J. D. Perez, The comprehensive inner magnetosphere-ionosphere model, *J. Geophys. Res. Space Physics*, *119*(9), 7522–7540, doi:10.1002/2014JA020239, 2014.

Freeman, J. W., T. P. O'Brien, A. A. Chan, and R. A. Wolf, Energetic electrons at geostationary orbit during the november 3-4, 1993 storm: Spatial/temporal morphology, characterization by a power law spectrum and, representation by an artificial neural network, *J. Geophys. Res.*, *103*(A11), 26,251–26,260, 1998.

Friedel, R., G. Reeves, and T. Obara, Relativistic electron dynamics in the inner magnetosphere - a review, *Journal of Atmospheric and Solar-Terrestrial Physics*, *64*(2), 265–282, 2002.

Friederich, U., D. Coca, S. A. Billings, and M. Juusola, Data modelling for analysis of adaptive changes in fly photoreceptors, *Neural Information Processing, PT 1, Proceedings*, *5863*, 34–38, 2009.

Gabrielse, C., V. Angelopoulos, A. Runov, and D. L. Turner, Statistical characteristics of particle injections throughout the equatorial magnetotail, *J. Geophys. Res. Space Physics*, *119*(4), 2512–2535, doi:10.1002/2013ja019638, 2014.

Ganushkina, N. Y., O. A. Amariutei, Y. Y. Shprits, and M. W. Liemohn, Transport of the plasma sheet electrons to the geostationary distances, *J. Geophys. Res. Space Physics*, *118*(1), 82–98, 2013.

Ganushkina, N. Y., M. W. Liemohn, O. A. Amariutei, and D. Pitchford, Low-energy electrons (5-50 kev) in the inner magnetosphere, *J. Geophys. Res. Space Physics*, *119*(1), 246–259, 2014.

Ganushkina, N. Y., O. A. Amariutei, D. Welling, and D. Heynderickx, Nowcast model for low-energy electrons in the inner magnetosphere, *Space Weather*, *13*(1), 2014SW001,098–, 2015.

Gubby, R., and J. Evans, Space environment effects and satellite design, *Journal of Atmospheric and Solar-Terrestrial Physics*, *64*(16), 1723–1733, 2002.

Guo, Y., L. Guo, S. Billings, and H.-L. Wei, An iterative orthogonal forward regression algorithm, *International Journal of Systems Science*, *46*(5), 776–789, doi: 10.1080/00207721.2014.981237, 2014.

Hanser, F. A., Eps/hepad calibration and data handbook, *Tech. rep.*, Tech. Rep. GOESN-ENG-048D, Assurance Technol. Corp., Carlisle, Mass., 2011.

Horne, R. B., S. A. Glauert, N. P. Meredith, D. Boscher, V. Maget, D. Heynderickx, and D. Pitchford, Space weather impacts on satellites and forecasting the earth's electron radiation belts with spacecast, *Space Weather*, *11*, 1–18, 2013a.

Horne, R. B., S. A. Glauert, N. P. Meredith, H. Koskinen, R. Vainio, A. Afanasiev, N. Y. Ganushkina, O. A. Amariutei, D. Boscher, A. Sicard, V. Maget, S. Poedts, C. Jacobs, B. Sanahuja, A. Aran, D. Heynderickx, and D. Pitchford, Forecasting the earth's radiation belts and modelling solar energetic particle events: Recent results from spacecast, *J. Space Weather Space Clim.*, *3*, A20, 2013b.

Kim, H.-J., and A. A. Chan, Fully adiabatic changes in storm time relativistic electron fluxes, *J. Geophys. Res.*, *102*(A10), 22,107–22,116, 1997.

Klimas, A. J., D. Vassiliadis, D. N. Baker, and D. A. Roberts, The organized nonlinear dynamics of the magnetosphere, *J. Geophys. Res.*, *101(A6)*, 13,089–13,113, 1996.

Koons, H. C., and D. J. Gorney, A neural network model of the relativistic electron flux at geosynchronous orbit, *J. Geophys. Res.*, *96*(A4), 5549–5556, 1991.

Krishnanathan, K., S. R. Anderson, S. A. Billings, and V. Kadirkamanathan, A data-driven framework for identifying nonlinear dynamic models of genetic parts, *ACS Synth. Biol.*, *1*(8), 375–384, doi:10.1021/sb300009t, 2012.

Leontaritis, I. J., and S. A. Billings, Input-output parametric models for non-linear systems part i: Deterministic non-linear systems., *Int. J. Control*, *41 (2)*, 303–328, 1985a.

Leontaritis, I. J., and S. A. Billings, Input-output parametric models for non-linear systems part ii: Stochastic nonlinear systems, *Int. J. Control*, *41 (2)*, 329–344, 1985b.

Li, X., Variations of 0.7-6.0 mev electrons at geosynchronous orbit as a function of solar wind, *Space Weather*, *2*(3), S03,006, 2004.

Li, X., D. N. Baker, M. Temerin, G. Reeves, R. Friedel, and C. Shen, Energetic electrons, 50 kev to 6 mev, at geosynchronous orbit: Their responses to solar wind variations, *Space Weather*, *3*(4), S04,001–, 2005.

Ling, A. G., G. P. Ginet, R. V. Hilmer, and K. L. Perry, A neural network-based geosynchronous relativistic electron flux forecasting model, *Space Weather*, *8*(9), S09,003–, 2010.

Lohmeyer, W., and K. Cahoy, Space weather radiation effects on geostationary satellite solid-state power amplifiers, *Space Weather*, *11*(8), 476–488, 2013.

Lohmeyer, W., A. Carlton, F. Wong, M. Bodeau, A. Kennedy, and K. Cahoy, Response of geostationary communications satellite solid-state power amplifiers to high-energy electron fluence, *Space Weather*, *13*(5), 2014SW001,147–, 2015.

Loto'aniu, T. M., H. J. Singer, J. V. Rodriguez, J. Green, W. Denig, D. Biesecker, and V. Angelopoulos, Space weather conditions during the galaxy 15 spacecraft anomaly, *Space Weather*, *13*(8), 484–502, Aug. 2015.

Mullen, E. G., M. S. Gussenhoven, D. A. Hardy, T. A. Aggson, B. G. Ledley, and E. Whipple, Scatha survey of high-level spacecraft charging in sunlight, *J. Geophys. Res.*, *91*(A2), 1474–1490, 1986.

O'Brien, T. P., and C. L. Lemon, Reanalysis of plasma measurements at geosynchronous orbit, *Space Weather*, *5*(3), doi:10.1029/2006sw000279, 2007.

Olsen, R. C., A threshold effect for spacecraft charging, *J. Geophys. Res.*, *88*(A1), 493–499, 1983.

Osthus, D., P. C. Caragea, D. Higdon, S. K. Morley, G. D. Reeves, and B. P. Weaver, Dynamic linear models for forecasting of radiation belt electrons and limitations on physical interpretation of predictive models, *Space Weather*, *12*(6), 426–446, 2014.

Paulikas, G. A., and J. B. Blake, Effects of the solar wind on magnetospheric dynamics: Energetic electrons at the synchronous orbit, *Quantitative Modeling of Magnetospheric Processes, Geophys. Monogr. Ser.*, *21*, 180–202, aGU, Washington, D. C., 1979.

Rastatter, L., M. M. Kuznetsova, A. Glocer, D. Welling, X. Meng, J. Raeder, M. Wiltberger, V. K. Jordanova, Y. Yu, S. Zaharia, R. S. Weigel, S. Sazykin, R. Boynton, H. Wei, V. Eccles, W. Horton, M. L. Mays, and J. Gannon, Geospace environment modeling 2008-2009 challenge: Dst index, *Space Weather*, *11*(4), 187–205, 2013.

Rigler, E. J., D. N. Baker, R. S. Weigel, D. Vassiliadis, and A. J. Klimas, Adaptive linear prediction of radiation belt electrons using the kalman filter, *Space Weather*, *2*(3), doi:10.1029/2003sw000036, 2004.

Sarno-Smith, L. K., B. A. Larsen, R. M. Skoug, M. W. Liemohn, A. Breneman, J. R. Wygant, and M. F. Thomsen, Spacecraft surface charging within geosynchronous orbit observed by the van allen probes, *Space Weather*, *14*(2), 151–164, doi: 10.1002/2015sw001345, 2016.

Sergeev, V., and N. Tsyganenko, Energetic particle losses and trapping boundaries as deduced from calculations with a realistic magnetic field model, *Planetary and Space Science*, *30*(10), 999–1006, 1982.

Subbotin, D. A., Y. Y. Shprits, and B. Ni, Long-term radiation belt simulation with the verb 3-d code: Comparison with crres observations, *J. Geophys. Res.*, *116*(A12), A12,210–, 2011.

Temerin, M., and X. Li, Dst model for 1995 - 2002, *J. Geophys. Res.*, *111*(A4), A04,221, 2006.

Thomsen, M. F., M. G. Henderson, and V. K. Jordanova, Statistical properties of the surface-charging environment at geosynchronous orbit, *Space Weather*, *11*(5), 237–244, doi:10.1002/swe.20049, 2013.

Turner, D. L., Y. Shprits, M. Hartinger, and V. Angelopoulos, Explaining sudden losses of outer radiation belt electrons during geomagnetic storms, *Nat Phys*, *8*(3), 208–212, 2012.

Wei, H. L., and S. A. Billings, An efficient nonlinear cardinal b-spline model for high tide forecasts at the venice lagoon, *Nonlinear Processes In Geophysics*, *13*(5), 577–584, 2006.

Wei, H. L., S. A. Billings, and M. Balikhin, Prediction of the dst index using multiresolution wavelet models, *J. Geophys. Res.*, *109*(A7), A07,212, 2004.

Wei, H.-L., S. A. Billings, A. Surjalal Sharma, S. Wing, R. J. Boynton, and S. N. Walker, Forecasting relativistic electron flux using dynamic multiple regression models, *Annales Geophysicae*, *29*(2), 415–420, doi:10.5194/angeo-29-415-2011, 2011.

Wrenn, G. L., D. J. Rodgers, and K. A. Ryden, A solar cycle of spacecraft anomalies due to internal charging, *Ann. Geophys.*, *20*(7), 953–956, 2002.

Zhao, Y., S. A. Billings, and A. F. Routh, Identification of the belousov-zhabotinskii reaction using cellular automata models, *International Journal of Bifurcation and Chaos*, *17*(5), 1687–1701, doi:10.1142/S0218127407017999, 2007.

Zhu, D., S. A. Billings, M. Balikhin, S. Wing, and D. Coca, Data derived continuous time model for the dst dynamics, *Geophys. Res. Lett.*, *33*(4), L04,101, 2006.

Zhu, D., S. A. Billings, M. A. Balikhin, S. Wing, and H. Alleyne, Multi-input data derived dst model, *J. Geophys. Res.*, *112*(A6), A06,205, 2007.

Model MLT	PE (%)	CC (%)	MSE	Var(J)
00	50.2	53.4	0.177	0.228
01	50.3	54.9	0.208	0.269
02	53.6	58.0	0.197	0.272
03	58.4	63.2	0.178	0.276
04	60.2	65.9	0.170	0.276
05	65.0	70.2	0.157	0.288
06	69.6	74.0	0.127	0.268
07	72.9	76.6	0.106	0.251
08	74.7	78.6	0.089	0.226
09	75.0	78.9	0.077	0.198
10	73.3	77.3	0.074	0.178
11	73.3	77.3	0.064	0.153
12	71.6	75.3	0.062	0.140
13	71.1	74.7	0.056	0.124
14	70.6	74.3	0.048	0.106
15	69.9	73.0	0.045	0.096
16	67.9	70.8	0.045	0.090
17	64.3	66.6	0.050	0.091
18	64.0	64.4	0.053	0.095
19	62.1	64.1	0.059	0.100
20	54.0	55.7	0.084	0.117
21	51.4	53.7	0.106	0.141
22	47.0	51.3	0.144	0.175
23	51.6	56.3	0.161	0.213

Table 1. Table showing the PE, CC, MSE for each MLT model and the variance of the measured electron flux.

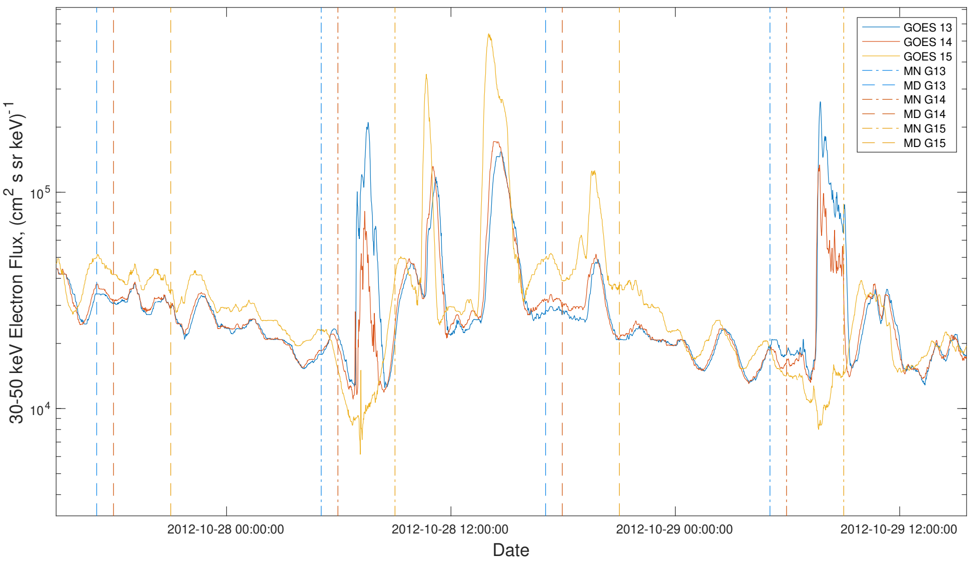

Figure 1. The 40 keV electron flux observed by the MAGED onboard GOES 13 (blue), 14 (orange) and 15 (yellow) between 27 October 2012 and 29 October 2012. The figure also shows when each of the spacecraft is at midday (GOES 13 - blue dashed, 14 - orange dashed, and 15 - yellow dashed) and midnight (GOES 13 - blue dot dashed, 14 - orange dot dashed, and 15 - yellow dot dashed).

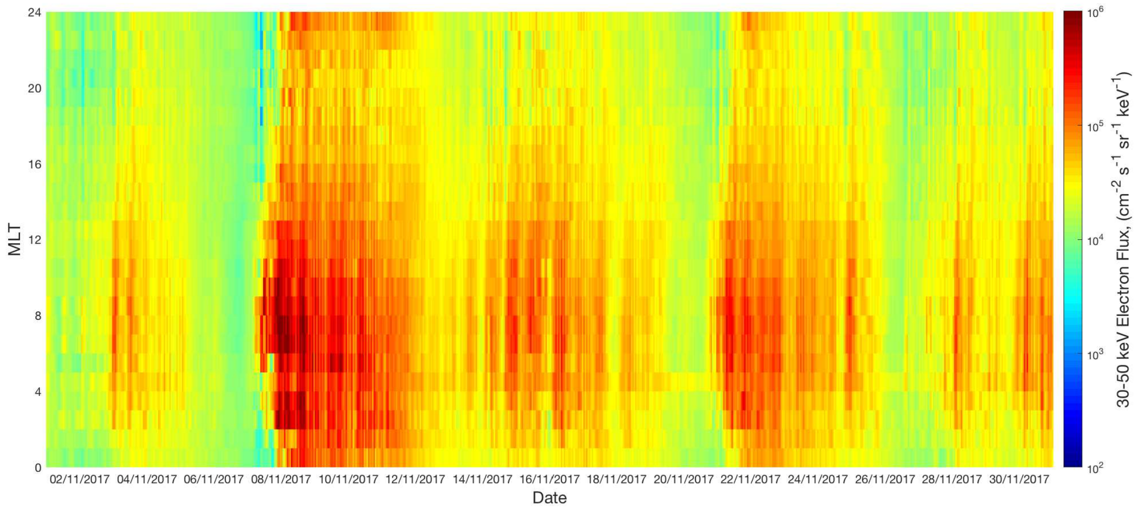

Figure 2. The model estimated 40 keV electron flux at all MLT from 1 November 2017 to 30 November 2017.

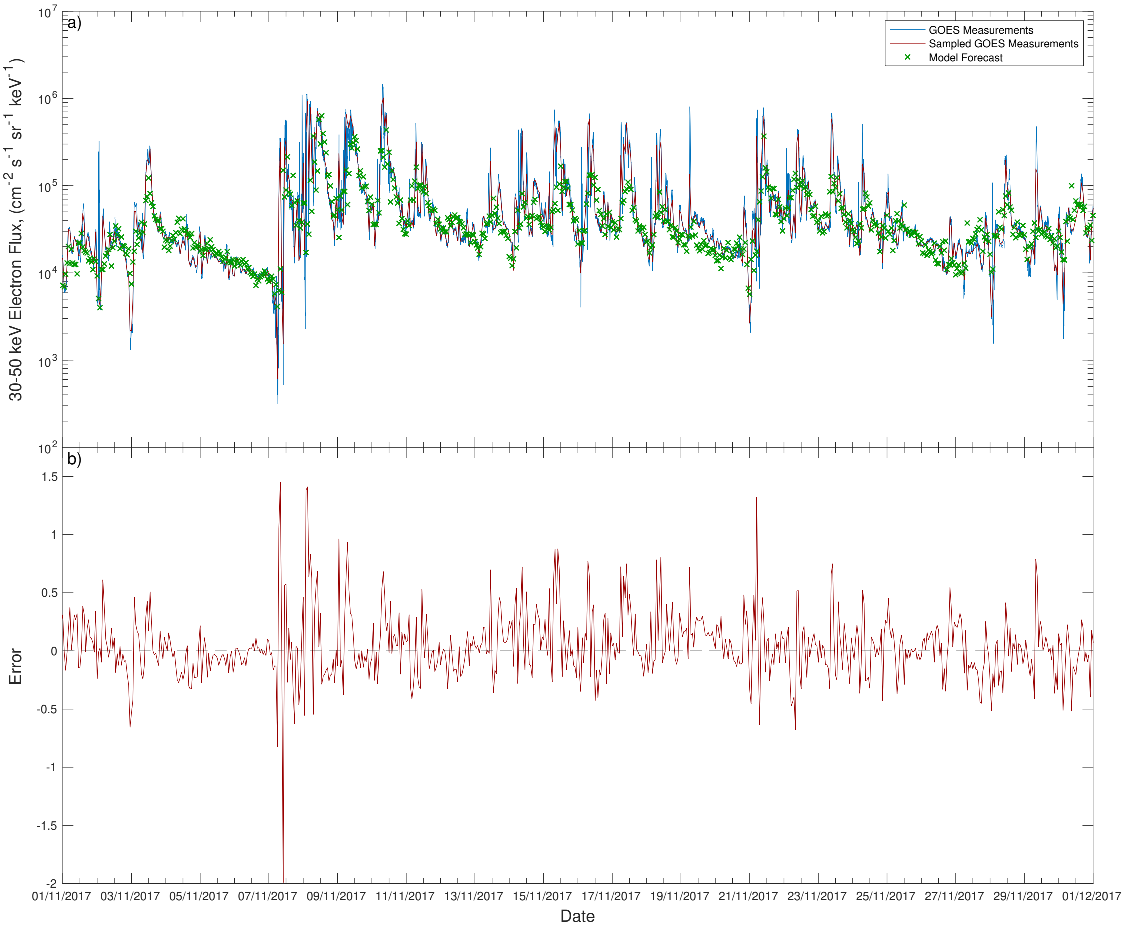

Figure 3. (a) The 40 keV electron flux observed by the MAGED onboard GOES 13 (blue), the sampled GOES 13 40 keV electron flux (red) and the model forecast at the GOES 13 location for November 2017. (b) The error between the sampled GOES 13 40 keV electron flux and the model forecast at the GOES 13 location for November 2017.

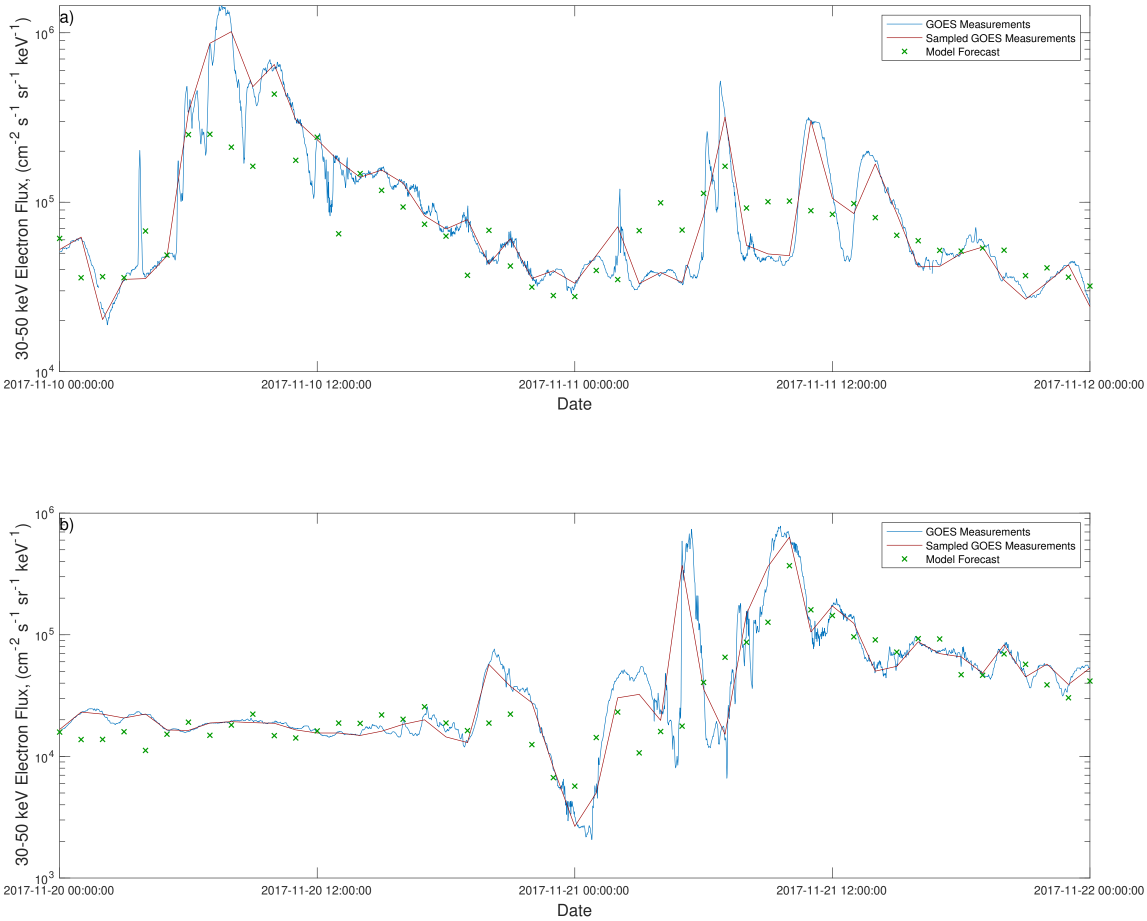

Figure 4. The 40 keV electron flux observed by the MAGED onboard GOES 13 (blue), the sampled GOES 13 40 keV electron flux (red) and the model forecast at the GOES 13 location for (a) 10-12 November 2017 and (b) 20-22 November 2017.

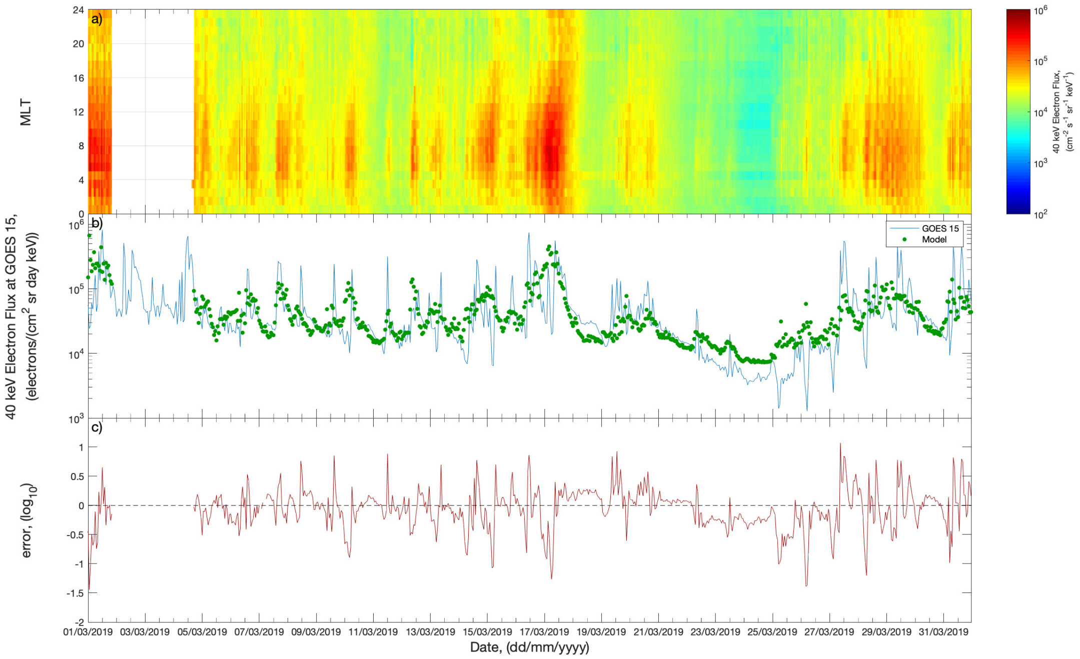

Figure 5. The real time output from the 40 keV electron flux model: (a) in MLT and time (b) at the GOES 15 location (green) vs GOES 15 data (blue), and (c) the error between the sampled GOES 15 40 keV electron flux and the model forecast at the GOES 15 location for March 2019